SnO2@TiO2 Heterojunction Nanostructures for Lithium-Ion Batteries and Self-Powered UV Photodetectors with Improved Performances

7 AUTHORS, INCLUDING:

Xiaojuan Hou
Inner Mongolia University of Science and T…
25 PUBLICATIONS **644** CITATIONS

SEE PROFILE

Bin Liu
National University of Singapore
390 PUBLICATIONS **9,082** CITATIONS

SEE PROFILE

Zhuoran Wang
McGill University
16 PUBLICATIONS **391** CITATIONS

SEE PROFILE

Guozhen Shen
Chinese Academy of Sciences
217 PUBLICATIONS **7,218** CITATIONS

SEE PROFILE

SnO$_2$@TiO$_2$ Heterojunction Nanostructures for Lithium-Ion Batteries and Self-Powered UV Photodetectors with Improved Performances

Xiaojuan Hou,[a] Xianfu Wang,[a] Bin Liu,[a] Qiufan Wang,[a] Zhuoran Wang,[a] Di Chen,*[a] and Guozhen Shen*[b]

To overcome the issue of inferior cycling stability and rate capacity for SnO$_2$ anode materials in lithium-ion batteries, an effective strategy is explored to prepare a hybrid material consisting of rutile SnO$_2$ nanoparticles and rutile TiO$_2$ nanorods, considering not only the small lattice mismatch to achieve a better composited lattice structure but also their superior synergistic effect in electrochemical performances. The as-prepared SnO$_2$@TiO$_2$ material, directly formed on a carbon cloth as a binder-free anode, exhibits a reversible capacity of 700 mAh g^{-1} after 100 discharge/charge cycles at 200 mA g^{-1}, as well as excellent cycling stability and rate capacity. After

being calcinated at high temperature, the produced hollow SnO$_2$@TiO$_2$ hybrid microtubes were directly used to fabricate photoelectrochemical (PEC) UV detectors for future devices with self-powered function. A high photocurrent response of 0.1 mA cm^{-2} was observed, together with an excellent self-powered and fast response and "visible blind" characteristics. Such a hybrid material could achieve a complementary effect in lithium-ion batteries and a superior band gap match in photovoltaic devices, and could consequently be extended to applications such as dye-sensitized solar cells and supercapacitors.

1. Introduction

Rechargeable lithium-ion batteries (LIBs) have been intensively studied during the past decade, and one of the research directions is to explore LIB anode materials with high reversible capacity, good rate capability and long cycle life. Until now, electrochemically active metal oxides, such as SnO$_2$,[1] TiO$_2$,[2] Co$_3$O$_4$,[3] MnO$_2$,[4] ZnCo$_2$O$_4$[5] and Fe$_2$O$_3$,[6–7] have emerged as the most promising candidates for the anode materials. Especially, SnO$_2$ has been extensively investigated as a novel anode material, owing to its high theoretical reversible capacity (~782 mAh g^{-1}), moderate operating voltage and good performance.[1,8-10] Unfortunately, practical applications of pure SnO$_2$ anodes are hampered by the low initial coulombic efficiency and poor material cycling stability arising from the large specific volume expansion during the discharge/charge processes, thus leading to poor contact with the current collector and an increase in the electrical resistance between particles.

To overcome these obstacles, the fabrication of SnO$_2$-based hybrid materials has been proved to be an effective strategy

to improve the electrochemical performance. Currently, composites containing carbonaceous materials, such as amorphous carbon,[8] CNT,[11] CMK,[10] and graphene,[12] have been regarded as the most promising choices owing to their excellent stability and high electronic conductivity. However, a key problem is that for most of the above cases, a long time is needed to achieve an active state or reach cycling stability. Hence, the search for better composite structures and proper hybrid nanomaterials to realize excellent performances is highly desired. Until now, SnO$_2$@TiO$_2$ heterostructures with good lattice and band-gap matches between rutile SnO$_2$ and rutile TiO$_2$ have been successfully prepared, and a promotion of the optoelectronic performance has also been realized.[13, 14]

In this report, SnO$_2$@TiO$_2$ heterostructures were successfully grown on a carbon cloth and were directly used as a binder-free anode to assemble coin cells with the inner carbon cloth as the current collector. The hybrid anode material exhibits a high initial coulombic efficiency of 80% and a reversible capacity of 700 mAh g^{-1} after 100 discharge/charge cycles, an excellent cycle stability and a good rate performance. Besides, high-performance photoelectrochemical (PEC) UV detectors were also fabricated by using high-temperature-calcinated SnO$_2$@TiO$_2$ hollow microtubes as the active material, which exhibited a high photocurrent, together with an excellent self-powered, fast response and "visible blind" characteristics. Our strategy for assembling this hybrid material opens up a new direction, considering not only the lattice match to achieve a better composite structure but also the synergistic effect between its basic properties.

[a] X. Hou, X. Wang, B. Liu, Q. Wang, Z. Wang, Prof. D. Chen
Wuhan National Laboratory for Optoelectronics
and School of Optical and Electronic Information
Huazhong University of Science and Technology
Wuhan 430074 (China)
E-mail: dichen@mail.hust.edu.cn

[b] Prof. G. Shen
State Key Laboratory for Superlattices and Microstructures
Institute of Semiconductors, Chinese Academy of Sciences
Beijing 100083 (China)
E-mail: gzshen@semi.ac.cn

Supporting information for this article is available on the WWW under
http://dx.doi.org/10.1002/celc.201300053.

2. Results and Discussion

Figure 1a shows the crystal structure of the tetragonal SnO_2 ($a=b=0.474$ nm, $c=0.319$ nm, center) and the tetragonal TiO_2 ($a=b=0.459$ nm, $c=0.296$ nm, right). The marked spheres represent Sn(Ti) atoms, and the other corresponds to O atoms. Having the same lattice structure, SnO_2 and TiO_2 only slightly differ in the lattice constant, which makes it possible to easily form into lattice matched composite structures. The crystal phases of the as-prepared products under different stages, namely, the as-prepared product (sample I), the product after annealing at 500 °C (sample II), and the product after calcination at 800 °C (sample III), were studied by X-ray diffraction (XRD), and the corresponding results are presented in Figure 1b. Sample I was found to consist of pure rutile SnO_2 (JCPDS 77-447) and rutile TiO_2 (JCPDS 89-8301, marked with a star) with carbon signals coming from the inner carbon-cloth substrate. Sample II, after annealing at 500 °C, showed a similar

XRD pattern to that of Sample I, except for the improved crystallinity. After annealing in air at 800 °C, the inner carbon cloth was removed and the sample (Sample III) consisted of only rutile SnO_2 and rutile TiO_2. The content of SnO_2 and TiO_2 could be calculated from Equation (1):

$$\omega_1 = 1/(1 + k_{21}I_2/I_1) \tag{1}$$

where k_{21} is the reference intensity value of the two materials, I_2 and I_1 are the corresponding diffraction intensity. Through calculated SnO_2 occupies the whole mass of 62%.

Figures 1c–e show the typical SEM images of the pure SnO_2 product grown on a carbon cloth, which was assembled by numerous SnO_2 nanoparticles with diameters of about 50–80 nm. SEM images of the sample after combination with TiO_2 (Sample II) are depicted in Figures 1f,g. From the images, we can see that numerous TiO_2 nanorods were grown on the surface of the SnO_2 nanoparticles. Because of the superior match of the lattice structure between rutile SnO_2 and TiO_2 (($aSnO_2$-$aTiO_2$)/$aSnO_2 = 3$% and ($cSnO_2$-$cTiO_2$)/$cSnO_2 = 7$%)), the hybrid material could be easily formed. According to our previous report,[15] TiO_2-seeded plays an important role in the following TiO_2 nanowires growth. In our case, the preformed SnO_2 nanoparticles were believed to act as the same role with TiO_2 seeds.

After sintered in air at 800 °C, the inner carbon cloth was successfully removed and the pure woven hybrid cloth forms with a little shrink in diameters of the assembled microtubes, as can be seen in Figure 1h (sample III). The inset in Figure 1h shows a magnified cross-section SEM image, where the morphologies of and the interface between TiO_2 nanorods and SnO_2 nanoparticles can be easily seen. A similar phenomenon was also found in our previous work using carbon cloth as the template.[15–16]

SnO_2 and TiO_2—two of the most common semiconductors—have wide applications in many areas, such as lithium-ion batteries, photodetectors, chemical sensors, catalysts and transistors. With good matched lattice structures, the current hybrid $SnO_2@TiO_2$ heterostructures may exhibit improved performances when used as active materials for lithium-ion batteries and photodetectors. To clarify this, the obtained hybrid samples on a carbon cloth were directly used as a binder-free anode with the inner carbon cloth as the current collector to assemble half-coin cells. Cyclic voltammetry (CV) was carried out to study the reactive mechanism. Figure 2 shows the first five CV curves of the $SnO_2@TiO_2$/C electrode at room temperature in the potential range of 0.01–3 V at a scan rate of 0.5 mV s^{-1}. The reduction peak (first sweep) located around 0.75 V can be attributed to the formation of Li_2O as well as the SEI film and the reduction of SnO_2 to Sn. As observed, there is no obvious peak which can be attributed to TiO_2 due to the small mass. The CV curves almost overlap from the second to fifth cycles, indicating that the cycling performance is considerably stable. To understand the reactive process in detail, a pure carbon cloth and SnO_2/C based batteries were also assembled to conduct CV measurements. Figure 3 shows the first CV curves made from different electrodes in the range of 0.01–3 V at a scan rate of 0.5 mV s^{-1}, from which we can find that the rela-
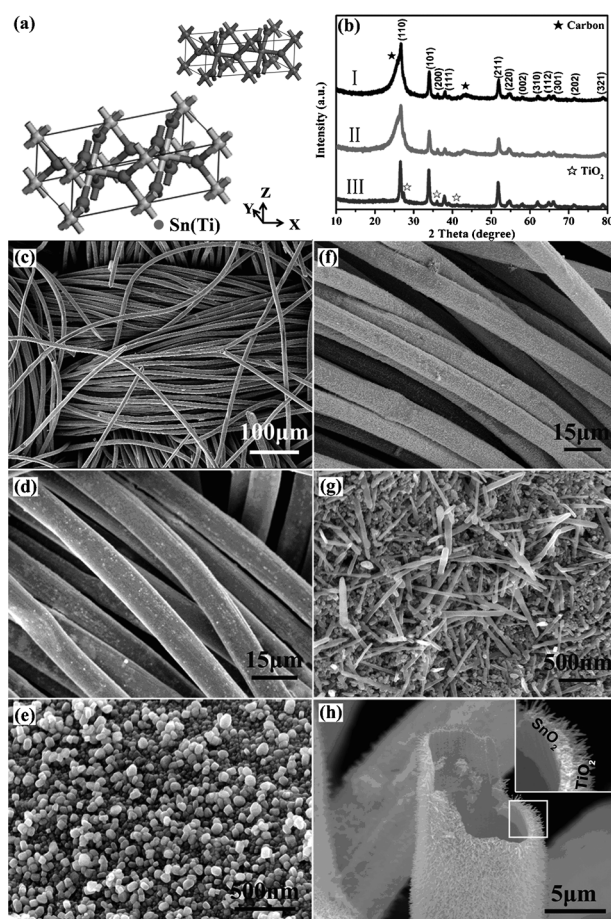

Figure 1. a) Crystal structures of tetragonal SnO_2 and TiO_2. b) XRD patterns of the as-obtained sample I (the as-prepared $SnO_2@TiO_2$/carbon cloth), II (500 °C treated $SnO_2@TiO_2$/carbon cloth), and III (the hollow $SnO_2@TiO_2$ microtube cloth). c–e) Typical SEM images of the prepared SnO_2 material on the carbon cloth, assembled by numerous nanoparticles. f,g) SEM images of sample II assembled by numerous SnO_2 nanoparticles and TiO_2 nanorods. h) Single $SnO_2@TiO_2$ microtube (sample III) with hollow characteristics. The inset shows an amplified cross-section SEM image, clearly presenting two different morphologies.
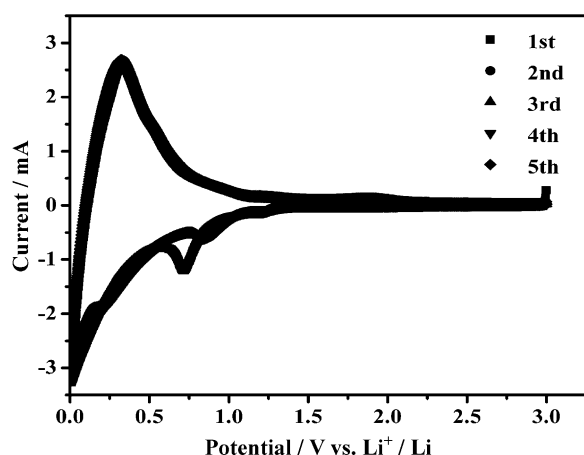
Figure 2. The first five current–voltage curves of the SnO$_2$@TiO$_2$/C electrode in the potential range of 0.01–3 V at a scan rate of 0.5 mV s^{-1}.

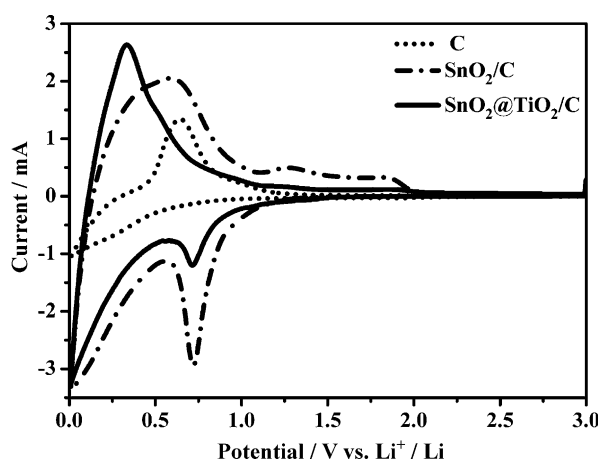**Figure 3.** The first current–voltage curves for an electrode made of C, SnO$_2$/C and SnO$_2$@TiO$_2$/C in the potential range of 0.01–3 V at a scan rate of 0.5 mV s^{-1}.

tive peak value around 0.75 V of the hybrid material is much smaller than that of pure SnO$_2$, indicating that after composite formation, the reaction is more reversible. The oxidation peak at around 0.6 V is somewhat shifted to lower voltages, which may be attributed to the influence of TiO$_2$. The pure carbon cloth contributed little to the whole CV curves. Hence, TiO$_2$ makes the electrochemical reaction more reversible and then promotes the cycling stability.

Galvanostatic cycling tests of the assembled cell were carried out to investigate its electrochemical performance, which was set in the potential range of 0.01–3 V at a current density of 200 mA g^{-1}. Figure 4a shows the voltage-specific capacity curves of the electrodes for the 1st, 2nd, 20th, 50th and 100th charge/discharge cycles. From these curves, it can be seen that there is no obvious discharge plateaus even in the first cycle, proving that the TiO$_2$ on the surface of SnO$_2$ has evident efficiency on the electrochemical reaction. Figure 4b shows the cycling performance of the SnO$_2$@TiO$_2$/carbon cloth at a current density of 200 mA g^{-1}. The initial coulombic efficiency is higher

than 80 % which is in accordance with the above CV curves. The coulombic efficiency in the following cycles remains as high as around 100 % and is relatively stable throughout the entire cycle tests, indicating the completeness of the SEI layer and good reversibility of the electrochemical reactions. Besides, the reversible capacity of the cell was found to be stable at around 700 mAh g^{-1}, even after 100 cycles, which nearly approaches the SnO$_2$ theoretical capacity (782 mAh g^{-1}). For comparison, electrode materials consisting of a pure carbon cloth and SnO$_2$/C were also studied. The areal capacities of the carbon cloth and the SnO$_2$@TiO$_2$/carbon cloth are presented in Figure S1 (inset), which demonstrates a low contribution of the carbon cloth. Under practical conditions, when coated with the hybrid material, the carbon cloth has a much lower contact area with the electrolyte and then could contribute even less to the whole capacity. Moreover, the pure carbon cloth displays a very low capacity of 55 mAh g^{-1} (Figure S1), slightly contributing to the whole capacity, whereas SnO$_2$/C presents a very fast capacity loss during the discharge/charge cycles and about 550 mAh g^{-1} after 100 cycles (Figure S2). As can be seen, the first discharge capacity of SnO$_2$/C is larger than that of the hybrid material, the main reason is the low capacity of TiO$_2$.

The electrochemical performance of the electrode was further studied at different current densities ranging from 100 to 1600 mA g^{-1}. Figures 4c,d show the corresponding rate performances, displaying that the specific capacity decreased from 800, 740, 630, 500, 320 to 245 mAh g^{-1} when the current density increased from 100, 200, 400, 800, 1200 to 1600 mA g^{-1}. The capacity was then reversed back to 700 mAh g^{-1} once the charge/discharge rate was set back to 100 mA g^{-1}, indicating the good rate performance of the current hybrid heterostructures. The corresponding coulombic efficiency is also plotted in Figure 4d. Although different current densities are gradually applied, the coulombic efficiency is always around 100 %, further demonstrating the excellent battery performance of the SnO$_2$@TiO$_2$/carbon cloth electrode. Based on the above results, we attributed the excellent cycling stability and rate performance to the high capacity of SnO$_2$, the good stability of TiO$_2$ and the superior match in the lattice level of the two semiconductors.

Since a lithium-ion battery needs to deliver a high power under some conditions, the Joule effect must be considered because large heat can be generated during the charge/discharge process at high current densities.[17] This process would heat up the battery, leading to an increase in the cell temperature. Meanwhile it is important to investigate the behavior of batteries at a low temperature, as this is necessary for practical applications. Therefore, it is crucial to study the battery's temperature-dependent performance. The performance of the assembled coin cells was further studied by putting the cells in temperatures (0–50 °C). The corresponding results are shown in Figure 5. It clearly shows that with the increased temperature ranging from 20 to 50 °C, the specific capacity slightly improved, since the resistance of the cell could be decreased and the ion mobility in the electrolyte can be enhanced with increased temperature.[18] When returning to initial temperature
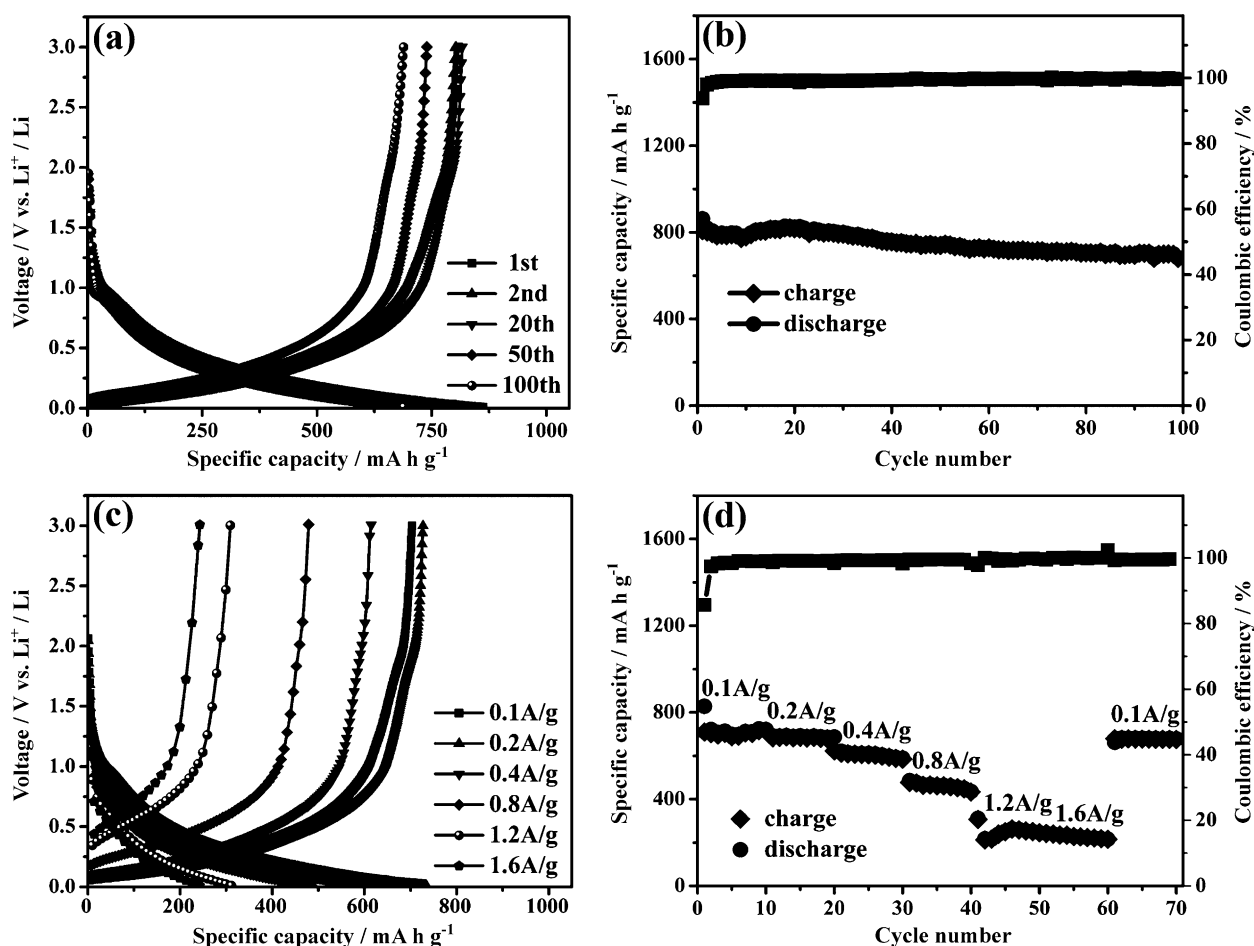
Figure 4. a) First, second, 20th, 50th and 100th charge/discharge curves of the $SnO_2@TiO_2/C$ electrode. b) Cycling performance of the battery at a current density of 200 mA g^{-1}. c) Galvanostatic charge/discharge curves at different current densities. d) Rate performance at different current densities.
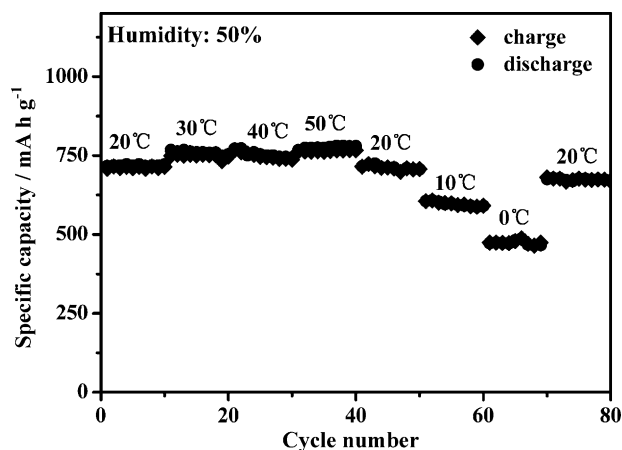

Figure 5. Cycling performance of the battery at a current density of 200 mA g^{-1} at different temperatures.

of 20 °C, the specific capacity reverted to its initial value. At lower temperature (0 and 10 °C), the specific capacity slightly decreased due to the low-temperature-induced high resistance of the cell. When the temperature was set back to room temperature, the capacity was also recovered. These results are in good accordance with previous reports.[19–21] Our results here

confirmed the excellent performance of the current cell with hybrid nanostructured heterojunction electrode.

To realize applications in some special areas, such as roll-up/bendable devices,[22–25] the current $SnO_2@TiO_2$ composite electrode was also used as binder-free anode to assemble a flexible full battery. Figure 6a presents the structure of the assembled flexible battery, consisting of a $LiCoO_2$/Al foil as the cathode, a $LiPF_6$-based electrolyte, a separator and a flexible plastic shell. The inset in Figure 6a is a photograph of the assembled full battery with excellent flexibility. It is well-known that the capacity of a commercial $LiCoO_2$ cathode is 40 mAh, which is much higher than the total capacity of the as-synthesized $SnO_2@TiO_2$ active materials (about 14 mAh). Hence, the final full batteries are anode-limited and the specific capacity and rate of the batteries referred to the mass of the negative $SnO_2@TiO_2$ structure electrodes. Figure 6b (inset) presents the voltage–capacity profiles of the as-assembled flexible full battery device for the 1st, 2nd, 10th and 25th charge/discharge cycles at a current density of 200 mA g^{-1} in the voltage window of 2–3.8 V. Detailed information about the cycling performance is presented in Figure 6b. The battery delivered a reversible capacity of about 750 mAh g^{-1} over 25 charge/discharge cycles, revealing a relatively good cycling performance
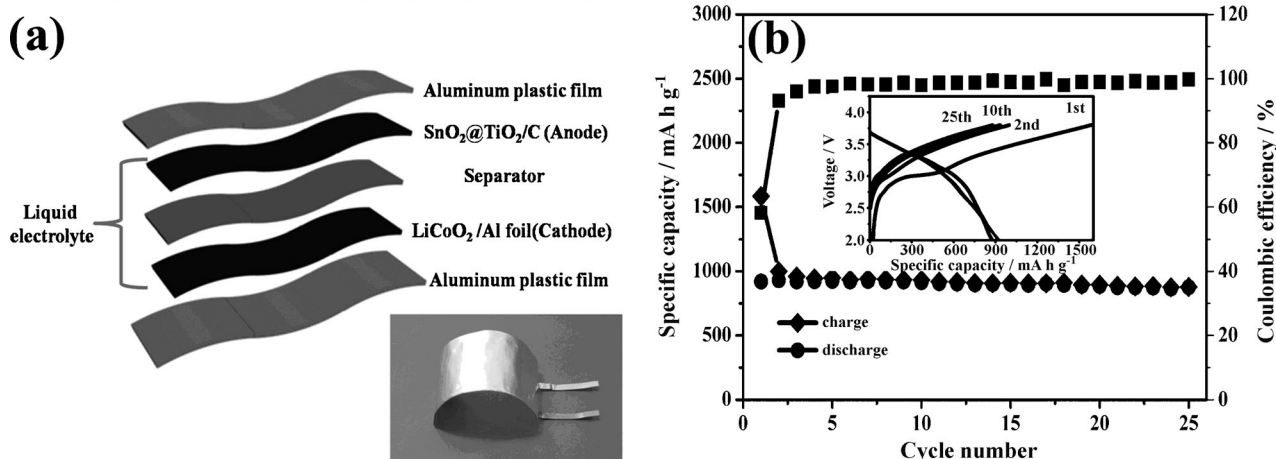
Figure 6. a) Structure of a $SnO_2@TiO_2/C$/liquid electrolyte/$LiCoO_2$ flexible lithium-ion battery. The inset shows an optical image of the full battery. b) Cycling performance of the flexible full battery up to 25 cycles at a current density of 200 mA g^{-1}. Inset: charge–discharge curves for the first, second, 10th and 25th cycles for the flexible battery.

of the device. The corresponding coulombic efficiency (CE) was also plotted in Figure 6b, which was found to remain at as high as around 100%, except for the first cycle. Benefiting from the excellent stability of TiO_2, and the high specific capacity of SnO_2, the composite exhibits a relatively high specific capacity and superior stability.

Considering the superior synergistic effect of the two semiconductors in a lithium-ion battery, we further investigated their application in photoelectrochemical (PEC) UV detectors. As is known, for a composite-based photoelectric device, the band gap structure of the assembled semiconductors plays an important role in its performance. The detailed band-gap structure of rutile SnO_2 and TiO_2 are studied, and the corresponding diagram is depicted in Figure 7. The valence band edge position of SnO_2/TiO_2 heterostructure was estimated according to the concepts of electronegativity.[26–27] Herein, the electronegativity of an atom is the arithmetic mean of the atomic electron affinity and the first ionization energy.[28] The valence-band po-

tentials of a semiconductor at the point of zero charge can be calculated by the following empirical equation [Eq. (2)]:[29–30]

$$E_{VB} = X\text{-}E^e + 0.5\ E_G \tag{2}$$

where E_{VB} is the valence-band-edge potential, X is the electronegativity of the semiconductor, which is the geometric mean of the electronegativity of the constituent atoms, E^e is the energy of free electrons on the hydrogen scale (about 4.5 eV), E_G is the band-gap energy of the semiconductor, and then E_{CB} can be determined by $E_{CB} = E_{VB} - E_G$. The X values for TiO_2 and SnO_2 are about 5.83 and 6.24 eV,[28] the band gap of TiO_2 and SnO_2 are 3.02 and 3.60 eV, and the E_{VB} of TiO_2 and SnO_2 were calculated to be 2.84 and 3.54 eV, respectively. Thus, the E_{CB} of TiO_2 and SnO_2 were estimated to be −0.18 and −0.06 eV, respectively. Hence, the composited $SnO_2@TiO_2$ structure can realize an efficient separation of electrons and holes, which accordingly enhance the lifetime of photogenerated electrons.

Photodetectors with different types have been widely investigated because of their extensive applications in environmental and biological research, optical communication, sensors and missile-launch detection.[31] Especially, self-powered photodetector is now the new trend to fit well for the future devices aiming at reduced size and weight.[32–35] Since the composite structure can efficiently enhance the electron lifetime, we also assembled it into self-powered photoelectrochemical UV detectors. The structure of the assembled device is presented in Figure 8a, which consists of the $SnO_2@TiO_2$ heterostructures bound to fluorine-doped tin oxide (FTO) as the photoanode and a platinized FTO glass as the cathode. When the heterostructured photoanodes were irradiated by UV light, photons with an energy higher than the band gap of SnO_2 or TiO_2 were transformed from the valence band to the conduction band and formed electron–hole pairs. Because of the good match of the band gap between SnO_2 and TiO_2, photogenerated electrons and holes can be separated efficiently. Electrons transfer quickly to the surface of SnO_2, while holes tend to go to the
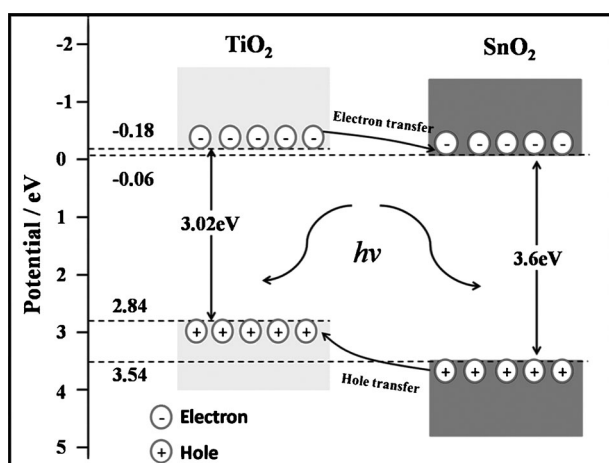

Figure 7. The energy-level diagram for TiO_2 and SnO_2 under illumination displays the separation of electron and hole.
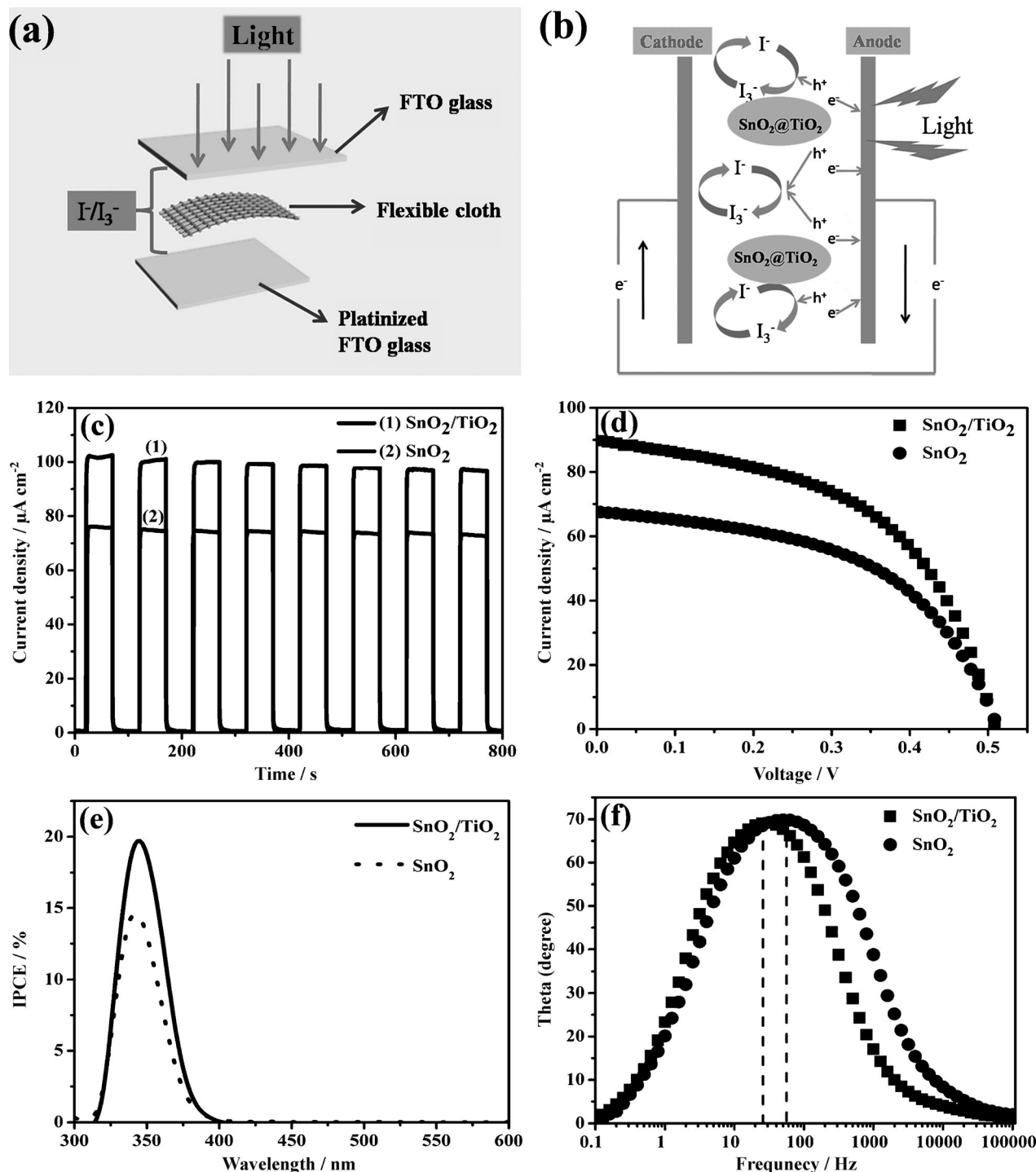
Figure 8. a) Structure of the photoelectrochemical cell (PEC). b) Detailed carrier-transferring process of the PEC under illumination. c) Photoresponse of different PEC detectors under a continuous 1.55 mW cm^{-2} UV-light rectangular pulse with a wavelength of 365 nm at a bias of 0 V. d) J–V curves for the PEC detector samples under 1.55 mW cm^{-2} irradiation with a wavelength of 365 nm. e) IPCE testing of the PEC photodetectors. f) EIS measurements under UV-light with a bias of V_{oc}.

surface of TiO$_2$, thus increasing the lifetime of the electrons. Then, the electrolyte establishes an intimate contact with nanocrystallites to realize a fast removal of holes, which will make the electrons travel more easily in the nanostructure network. During the light illumination, the photocurrent can be continuously regenerated owing to I$^-$/I$_3^-$ redox couples. As

soon as the electron–hole pairs are created, the holes will be quickly removed by I$^-$, described as follows:

$$3I^- + 2h^+ \rightarrow I_3^-$$
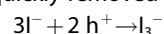
The separated electrons transport through the nanocrystalline network and are collected easily by the FTO glass electrode, which can arrive at the counter electrode through the external circuitry. The electrolyte is thus recovered to I$^-$ by the

electrons gathered at the cathode owing to the catalysis of Pt which is ready to remove another hole from the surface of the semiconductor:

$$I_3^- + 2e^- \rightarrow 3I^-$$
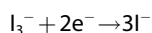
The detailed schematic diagram of the carrier-transferring process is displayed in Figure 8b.

We first investigated the current response by introducing a continuous 365 nm UV light rectangle pulse with an on–off interval of 50 s at a bias of 0 V supplied by a 1.55 mW cm^{-2} hand lamp as a light source. A certain area of 0.5×1 cm^2 was applied during the measurement to get the photocurrent density value. The photocurrent response curves are presented in Figure 8c, indicating a good stability of the PEC photodetectors. The SnO$_2$@TiO$_2$ heterostructures showed an obvious enhancement of the photocurrent, reaching 0.1 mA cm^{-2} compared to the pure SnO$_2$ cloth. Figure 8d display the J–V curves under UV light, corresponding well with the photocurrent-response curves shown in Figure 8c. The higher photocurrent can be explained by the higher incident-photon to current (IPCE) value shown in Figure 8e. The J–V characteristics in the dark for the PEC photodetector were also measured (Figure S3), showing very low current densities. To investigate the recombination properties, we introduced electrochemical impedance spectroscopic (EIS) testing under 365 nm UV light with open-circuit-voltage bias to analyze the electron-transport information between the interfaces. Figure 8f displays the corresponding Bode phase plots, from which we can get the characteristic peak frequency f_{peak} for the devices. The electron lifetime can be estimated according to Equation (3):

$$\tau \approx 1/\omega_{peak} = 1/(2\pi f_{peak}) \tag{3}$$

The lower characteristic peak frequency for the SnO$_2$@TiO$_2$ heterostructures represents the higher electron lifetime. Hence, it proves the outstanding electron transferring property of the SnO$_2$@TiO$_2$ heterostructures. Meanwhile, such heterostructures can achieve efficient separation of electrons and holes. Therefore long lived charge separation and good transport were achieved in the SnO$_2$@TiO$_2$ heterostructures, which lead to a greatly enhanced photoresponse compared to the pure SnO$_2$ cloth.

3. Conclusions

In summary, we successfully synthesized a SnO$_2$@TiO$_2$/carbon cloth material exhibiting superior electrochemical performances, featuring a high reversible capacity, an excellent rate capability and a long cycling life. Our strategy to employ the synergistic couple of SnO$_2$ with high capacity and TiO$_2$ with excellent cycling stability is successful in designing advanced anode materials. The SnO$_2$@TiO$_2$ heterostructures were also assembled into self-powered UV photodetectors, which present outstanding photovoltaic properties, a good ultraviolet selectivity, and a high and fast response. The superior performance is attributed to the excellent band-gap match between rutile SnO$_2$ and rutile TiO$_2$. The superior synergistic effect resulted in a greatly improved performance, and such a structure may

find other interesting applications, such as dye-sensitized solar cells, supercapacitors, photocatalysts and so on.

Experimental Section

Growth of SnO$_2$ on a Carbon Cloth

To grow SnO$_2$ on a carbon cloth, commercially available carbon cloths were first cut into the desired sizes and sequentially cleaned with acetone, deionized water, and ethanol. The pre-cleaned carbon cloths were seeded by immersion in a 0.1 M SnCl$_4$ solution overnight, and then heated in air at 450 °C for 30 min. A piece of the seeded carbon cloth was placed in a Teflon-lined stainless-steel autoclave containing a mixture of 0.2 g of SnCl$_2$·2H$_2$O and 34 mL of diluted hydrochloric acid (0.65 M). The sealed autoclave was heated in an oven at 180 °C for 20 h. Once the reaction finished, the cloth was washed with deionized water and ethanol and then dried in air.

Preparation of SnO$_2$@TiO$_2$ Hybrid Heterojunctions

The above SnO$_2$ coated carbon cloth was placed within a digestion vessel containing a mixture of 12 mL deionized water, 12 mL hydrochloric acid (36.6–38% by weight) and 0.5 mL tetrabutyl titanate. The reaction was performed via a microwave-assisted hydrothermal method at 180 °C for 1 h. After reaction, the product was dried and then sintered at 500 °C for 1 h to improve the crystallinity. The SnO$_2$@TiO$_2$ hollow microtubes were prepared by annealing the above product at 800 °C in air for 3 h to remove inner carbon cloths.

Characterization

X-ray diffraction patterns were obtained on an X-ray diffractometer (X'Pert PRO, PA Nalytical B.V., the Netherlands) with radiation from a Cu target (kα, λ = 0.15406 nm). Field-emission scanning electron microscopy (FESEM) images were obtained with an FEI Siron 200 (10 kV).

Electrochemical Measurements

The electrochemical properties of the as-prepared SnO$_2$@TiO$_2$/carbon cloth products were studied by assembling them as the CR2032 coin-type half cells in an argon-filled glove box with both the moisture and oxygen concentrations below 1 ppm at room temperature. The structure of the coin cell consists of a lithium foil as the counter electrode and reference electrode, celgard 2300 as the separator membrane and a piece of the prepared product on a carbon cloth as the working electrode without any conductive agent or polymeric binder. The electrolyte involves a solution of 1 M LiPF$_6$ in a mixture of ethylene carbonate (EC) and dimethyl carbonate (DMC) (v/v = 1:1). Flexible full battery was also fabricated by using LiCoO$_2$/Al foil as the counter electrode, aluminum plastic films as flexible shells, and the SnO$_2$@TiO$_2$/carbon cloth as the working electrode. The loading density of the active material was calculated to be about 1.6 mg cm^{-2} for SnO$_2$ and 2 mg cm^{-2} for SnO$_2$@TiO$_2$. The galvanostatic discharge/charge measurements and rate performances were carried out on a Land Battery Measurement System (Land, China) at different current densities with a voltage window of 0.01–3.00 V for the coin-type half cells and 2–3.8 V for the full batteries.

PEC Photodetector Characterization

To fabricate PEC UV detectors, the hollow $SnO_2@TiO_2$ microtube cloths were directly used as the photoanode. Isopropyl titanate was used as a binder to connect the hollow $SnO_2@TiO_2$ microtube cloth onto an FTO glass. The counter electrode was platinized by coating with a drop of isopropanol solution of H_2PtCl_6 followed by annealing at 400 °C for 20 min and repeated twice. Then the photoanode and cathode were sandwiched using thermoplastic 'Surlyn' as a spacer and followed by injecting an electrolyte containing DMPII (1.0 M), LiI (0.1 M), I_2 (0.12 M), and 4-TBP (0.5 M) in methoxypropionitrile to finish the device fabrication. Photocurrent and electrochemical impedance measurements were conducted under ultraviolet hand lamp conditions providing a power density of 1.55 mW cm^{-2}, and with an Autolab (model AUT84315) to realize automatic data acquisition. IPCE was measured by an IPCE testing system (Newport).

Acknowledgements

[1] Z. Y. Wang, Z. C. Wang, S. Madhavibc, X. W. Lou, *J. Mater. Chem.* **2012**, *22*, 2526–2531.
[2] S. J. Ding, J. S. Chen, D. Y. Luan, F. Y. C. Boey, S. Madhavi, X. W. Lou, *Chem. Commun.* **2011**, *47*, 5780–5782.
[3] L. M. Wang, B. Liu, S. H. Ran, H. T. Huang, X. F. Wang, B. Liang, D. Chen, G. Z. Shen, *J. Mater. Chem.* **2012**, *22*, 23541–23546.
[4] W. Xiao, J. S. Chen, X. W. Lou, *CrystEngComm* **2011**, *13*, 5685–5687.
[5] B. Liu, J. Zhang, X. F. Wang, G. Chen, D. Chen, C. W. Zhou, G. Z. Shen, *Nano Lett.* **2012**, *12*, 3005–3011.
[6] L. Yu, Z. Y. Wang, L. Zhang, H. B. Wu, X. W. Lou, *J. Mater. Chem. A* **2013**, *1*, 122–127.
[7] X. Jia, J. J. Chen, J. H. Xu, Y. N. Shi, Y. Z. Fan, M. S. Zheng, Q. F. Dong, *Chem. Commun.* **2012**, *48*, 7410–7412.
[8] X. W. Lou, J. S. Chen, P. Chen, L. A. Archer, *Chem. Mater.* **2009**, *21*, 2868–2874.
[9] Z. Y. Wang, D. Y. Luan, F. Y. C. Boey, X. W. Lou, *J. Am. Chem. Soc.* **2011**, *133*, 4738–4741.
[10] F. Han, W. C. Li, M. R. Li, A. H. Lu, *J. Mater. Chem.* **2012**, *22*, 9645–9651.
[11] S. J. Ding, J. S. Chen, X. W. Lou, *Adv. Funct. Mater.* **2011**, *21*, 4120–4125.
[12] S. J. Ding, D. Y. Luan, F. Y. C. Boey, J. S. Chen, X. W. Lou, *Chem. Commun.* **2011**, *47*, 7155–7157.
[13] X. M. Wu, S. C. Zhang, L. L. Wang, Z. J. Du, H. Fang, Y. H. Ling, Z. H. Huang, *J. Mater. Chem.* **2012**, *22*, 11151–11158.
[14] X. D. Li, C. T. Gao, H. G. Duan, B. A. Lu, Y. Q. Wang, L. L. Chen, Z. X. Zhang, X. J. Pan, E. Q. Xie, *Small* **2013**, DOI: 10.1002/smll.201202408.
[15] Z. R. Wang, H. Wang, B. Liu, W. Z. Qiu, J. Zhang, S. H. Ran, H. T. Huang, J. Xu, H. W. Han, D. Chen, G. Z. Shen, *ACS Nano* **2011**, *5*, 8412–8419.
[16] B. Liu, Z. R. Wang, Y. Dong, Y. G. Zhu, Y. Gong, S. H. Ran, Z. Liu, J. Xu, Z. Xie, D. Chen, G. Z. Shen, *J. Mater. Chem.* **2012**, *22*, 9379–9384.
[17] K. Zaghib, J. B. Goodenough, A. Mauger, C. Julien, *J. Power Sources* **2009**, *194*, 1021–1023.
[18] C. Masarapu, H. F. Zeng, K. H. Hung, B. Q. Wei, *ACS NANO* **2009**, *3*, 2199–2206.
[19] J. Yan, A. Sumboja, E. Khoo, P. S. Lee, *Adv. Mater.* **2011**, *23*, 746–750.
[20] D. Luo, G. S. Li, C. Yu, L. S. Yang, J. Zheng, X. F. Guan, L. P. Li, *J. Mater. Chem.* **2012**, *22*, 22233–22241.
[21] J. Shim, R. Kostecki, T. Richardson, X. Song, K. A. Striebel, *J. Power Sources* **2002**, *112*, 222–230.
[22] X. F. Wang, W. F. Song, B. Liu, G. Chen, D. Chen, C. W. Zhou, G. Z. Shen, *Adv. Funct. Mater.* **2013**, *9*, 1202–1209.
[23] Z. Liu, H. T. Huang, B. Liang, X. F. Wang, Z. R. Wang, D. Chen, G. Z. Shen, *Optics Express* **2012**, *20*, 2982–2991.
[24] P. C. Chen, G. Z. Shen, S. Sukcharoenchoke, C. W. Zhou, *Appl. Phys. Lett.* **2009**, *94*, 043113–3.
[25] H. Gwon, H. S. Kim, K. U. Lee, D. H. Seo, Y. C. Park, Y. S. Lee, B. T. Ahna, K. Kang, *Energy Environ. Sci.* **2011**, *4*, 1277–1283.
[26] A. H. Nethercot, *Phys. Rev. Lett.* **1974**, *33*, 1088–1091.
[27] Y. I. Kim, S. J. Atherton, E. S. Brigham, T. E. Mallouk, *J. Phys. Chem.* **1993**, *97*, 11802–11810.
[28] M. A. Butler, D. S. Ginley, *J. Electrochem. Soc.* **1978**, *125*, 228–232.
[29] X. P. Lin, J. C. Xing, W. D. Wang, Z. C. Shan, F. F. Xu, F. Q. Huang, *J. Phys. Chem. C* **2007**, *111*, 18288–18293.
[30] W. D. Wang, F. Q. Huang, X. P. Lin, *Scr. Mater.* **2007**, *56*, 669–672.
[31] G. Konstantatos, E. H. Sargent, *Nat. Nanotechnol.* **2010**, *5*, 391–400.
[32] S. Xu, Y. Qin, C. Xu, Y. G. Wei, R. S. Yang, Z. L. Wang, *Nat. Nanotechnol.* **2010**, *5*, 366–373.
[33] Z. L. Wang, *Adv. Funct. Mater.* **2008**, *18*, 3553–3567.
[34] X. F. Wang, B. Liu, Q. F. Wang, W. F. Song, X. J. Hou, D. Chen, Y. B. Cheng, G. Z. Shen, *Adv. Mater.* **2013**, *25*, 1479–1486.
[35] Z. R. Wang, S. H. Ran, B. Liu, D. Chen, G. Z. Shen, *Nanoscale* **2012**, *4*, 3350–3358.